Kennett, B. L. N., Sippl, C. (2018): Lithospheric discontinuities in Central Australia. - *Tectonophysics*, *744*, pp. 10—22.

DOI: http://doi.org/10.1016/j.tecto.2018.06.008

# Lithospheric discontinuities in Central Australia

B.L.N. Kennett[a], C. Sippl[b]

[a] *Research School of Earth Sciences, The Australian National University, Canberra ACT 2601, Australia*
[b] *Section Lithosphere Dynamics, Deutsches GeoForschungsZentrum, Telegrafenberg, 14473 Potsdam, Germany*

---

## Abstract

Lithospheric discontinuities are elusive, with properties that are strongly frequency dependent. Results from a temporary deployment of broadband stations along a north-south transect through Central Australia, and the permanent arrays ASAR and WRA, are used to evaluate the spatial coherence of lithospheric features, particularly mid-lithospheric discontinuities. We exploit stacked station autocorrelograms that provide an estimate of *P*-wave reflectivity beneath stations, with imaging methods exploiting teleseismic arrivals. We use both common conversion point (CCP) stacking from *Ps* receiver functions and reflection point imaging using the autocorrelation of the *P* wavetrain. The results tie well for the Moho and have a good general correspondence for deeper levels. Although indications of mid-lithospheric discontinuities from changes in the frequency of reflectivity occur at similar depths, the spatial continuity of specific features at high frequency (around 2 Hz) is of the order of 10-15 km. Broader trends can be tracked across the profile, but no strong lithospheric interfaces can be mapped, except for a south dipping feature traversing the lithosphere on the southern part of the profile that is likely to be a former mantle detachment zone.

*Key words:* Lithospheric discontinuities; Moho ; Central Australia; Autocorrelograms; Receiver Functions

---

*URL:* Brian.Kennett@anu.edu.au (B.L.N. Kennett)

## 1. Introduction

Full characterisation of the seismic structure of the lithosphere requires the integration of many different classes of data and analysis techniques. The broad scale features can be sought with surface wave tomography, which can provide information on both seismic shear wavespeed and anisotropy. The vertical gradients of wavespeed can then be used to place constraints on the transition from the lithosphere to the asthenosphere (e.g., Yoshizawa and Kennett, 2015). Variations in the distribution of azimuthal and radial anisotropy with depth tie to the presence of lithospheric discontinuities (e.g., Yuan and Romanowicz, 2010; Yuan and Levin, 2014; Yoshizawa, 2014). Higher-frequency information from body-waves provides more constraints on finer-scale structure, either in transmission or refraction. For the Australian continent, Kennett et al. (2017) have shown how a multi-scale heterogeneity model can be constructed that is compatible with a wide range of seismological observations. This model incorporates deterministic large-scale structure and stochastic representations of intermediate and fine scales. The amplitude of the smaller scale variations are modest ($<$ 1%). These rapid variations in seismic wavespeeds at short scales ($\sim$ 10-20 km horizontally, $\sim$0.5 km vertically) superimposed on slower background variations are able to produce apparent discontinuities from constructive interference, which show distinct frequency dependence. For low-frequency incident waves, receiver functions can be interpreted in terms of models with a few major discontinuities, though contrasts may be exaggerated.

We here use data from a relatively dense profile of portable seismic instruments through Central Australia from the BILBY experiment (2008-2010) to examine the continuity and character of lithospheric discontinuities. The north-south BILBY profile passes the permanent array stations at Warramunga (WRA) and Alice

Springs (ASAR), affording the opportunity to look locally at structures in more detail. We combine information from surface wave analysis, receiver functions and autocorrelation techniques to track the discontinuities and examine their expression in different frequency bands. Sippl (2016) has presented detailed receiver-function analysis for this profile so we already have strong constraints on the crust-mantle transition. We therefore focus on the continuity of potential mid-lithospheric discontinuities, and the character of the lithosphere-asthenosphere transition.

## 2. Tectonic setting

The BILBY profile spans from the northern part of the South Australian Craton to the North Australian Craton, crossing the complex central Australian belt which has been deformed in the 570-530 Ma Petermann Orogeny and the 450-300 Ma Alice Springs Orogeny (Figure 1). The Arunta and Musgrave Blocks have been uplifted in these orogenic events, leaving jumps in crustal thickness of over 10 km, summarised by Korsch and Doublier (2016), and consequent major gravity anomalies (Figure 1). As noted by Fishwick and Reading (2008) and Kennett and Iaffaldano (2013), the mantle lithosphere beneath the Central Australian zone does not show any notable evidence of the deformation cycles. Indeed shear wavespeeds at around 100 km depth are among the highest anywhere on the continent. Wavespeeds above 80 km are somewhat reduced compared with the average for the cratonic regions, but the distribution in images generated with Pn wave tomography is somewhat patchy (Sun and Kennett, 2016a).

Sippl (2016) provides an account of the tectonic history of the region, so here we concentrate on the features along the profile of portable instruments. The southern end of the denser station deployment lies in the northern part of the South Australian Craton, which mainly consists of Paleo- and Meso-proterozoic rocks

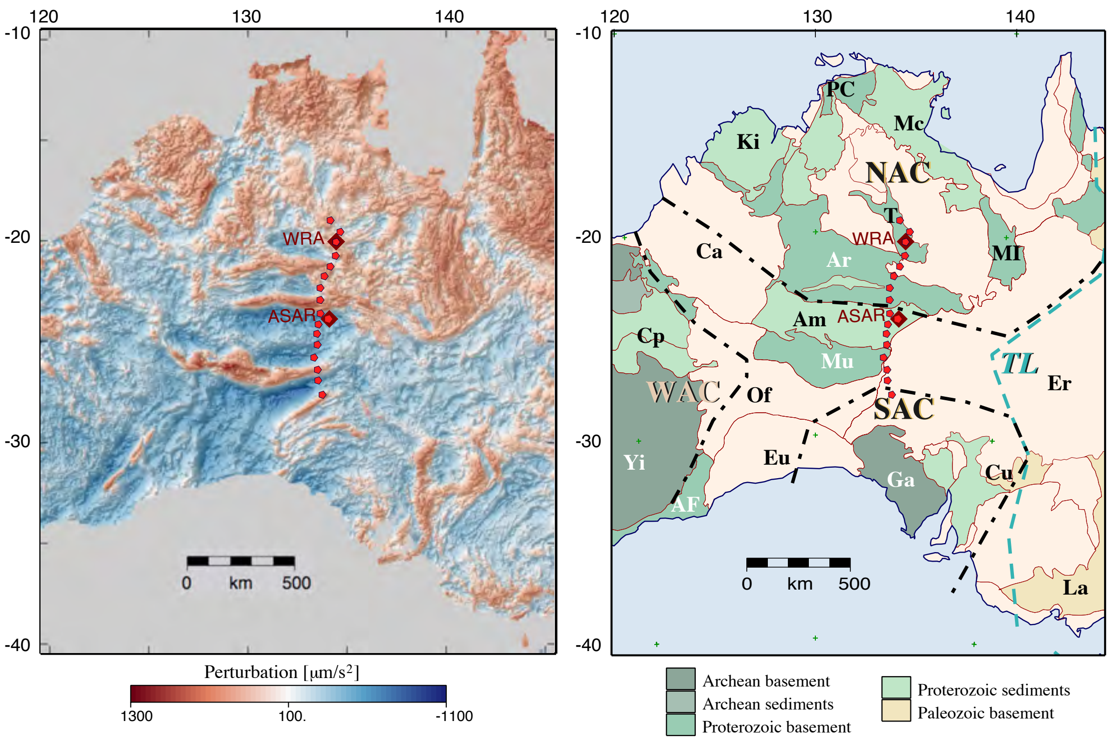


Figure 1: (a) Free-air gravity anomalies in central Australia (data from Geoscience Australia). (b) Simplified representation of the main tectonic features of central Australia. Chain-dotted lines mark outlines of the major cratons (NAC - North Australian Craton, SAC- South Australian Craton, WAC- West Australian Craton). The Tasman line (TL) in dashed cyan is based on the reinterpretation by Direen and Crawford (2003). Key to marked features: AF - Albany-Fraser Belt, Ar - Arunta Block, Am - Amadeus Basin, Ca - Canning Basin, Cp - Capricorn Orogen, Cu - Curnamona Craton, Er - Eromanga Basin, Eu - Eucla Basin, Ga - Gawler Craton, Ki - Kimberley Block, La - Lachlan Orogen, Mc - MacArthur Basin, MI - Mt. Isa Block, Mu - Musgrave Block, Of - Officer Basin, PC - Pine Creek Inlier, T - Tennant Creek Block, Yi - Yilgarn Craton. The location of the portable seismic stations from the BILBY experiment used for tracking lithospheric discontinuities are shown in red, along with the permanent stations WRA and ASAR.

around a small nucleus of Archean meta-sedimentary and volcanic rocks. The dominantly Meso-proterozoic Musgrave province has been uplifted, and around the line of profile displays a crustal pop-up structure with middle to lower crustal rocks raised by around 10 km compared with the surroundings (e.g., Korsch and Doublier, 2016). This feature produces the southernmost of the major east-west gravity anomalies in Figure 1a.

The basement rocks of the Arunta province probably underlie the relatively thick sediments (up to 8km) of the Amadeus basin. Lower crustal rocks are brought close to the surface by the steeply dipping Redbank Shear zone, with a sharp Moho step up to the north (Korsch et al., 1998). This thrust is thought to have been reactivated during the Alice Springs orogeny. This 20 km Moho step also produces a strong east-west oriented gravity anomaly. The Paleo-proterozoic rocks continue north of the Arunta province in the Tennant Creek Inlier traversed by the profile. Sippl (2016) suggests the presence of a further Moho step just south of station WRA (Figure 1).

## 3. Receiver-based studies

Much of the available information on lithospheric discontinuities comes from the application of receiver function methods. The converted *S* waves from incident teleseismic *P* waves are commonly used to determine crustal thickness, but frequently contamination by crustal multiples obscures the potential signal from discontinuities within the mantle component of the lithosphere. In consequence, incident *S* waves have been favoured because the *P* conversions arrive ahead of the crustal multiples. From the interpretation of such *Sp* receiver functions there have been widespread reports of a *S* velocity reduction at depths around 80–120 km (e.g., Abt et al., 2010; Chen et al., 2014; Ford et al., 2010; Tharimena et al., 2016). Such depths lie within the lithosphere for stable shield regions and the features have been identified as mid-lithosphere discontinuities (MLD) (e.g., Abt et al., 2010; Chen et al., 2014; Selway et al., 2015). In tectonically active areas with thin lithosphere, the wavespeed reduction has been interpreted as the lithosphere-asthenosphere boundary (LAB).

Normally receiver function studies of the deeper lithosphere exploit lower frequencies so as to reduce noise and concentrate attention on the dominant structures (e.g., 0.03–1 Hz for incident *P*, and 0.03–0.5 Hz for incident *S*). For such frequency bands, the vertical resolution is about 15 km.

An alternative approach to explore lithospheric discontinuities is to extract *P* wave reflectivity from continuous or earthquake waveforms at higher frequencies (0.5–4 Hz) that allow resolution of finer-scale lithospheric structures, down to $\sim$1 km in depth extent (Kennett, 2015). The stacked autocorrelation of ambient noise segments corresponds to the Green's function for coincident source and receiver at the location of a seismic station, whilst the autocorrelation of transmitted waves recorded at the free surface extracts the reflection response beneath the station. In consequence, stacked autocorrelograms of continuous seismic data provide estimates of the *P* reflectivity beneath a station (Gorbatov et al., 2013), with the possibility of some influence from local scattering. Such stacked autocorrelograms have been applied across Australia to image the Moho discontinuity as the base of crustal reflectivity (Kennett et al., 2015), and to examine the nature of the lithosphere-asthenosphere transition (Kennett, 2015).

Sun and Kennett (2016b) have pointed out the advantages of working directly with the immediate coda of *P* for teleseisms, for which the autocorrelation of the vertical component transmitted waves provides a direct estimate of the *P* reflectivity beneath the station for the slowness of the incident wave. Stacking over a span of slownesses yields estimates of the *P* reflection response with high signal-to-noise. The same portion of the seismogram is employed as in receiver function analysis, indeed the cross-correlation of the vertical and radial components provides an alternative route to look at conversions. Sun and Kennett (2017) have demonstrated the use of teleseismic autocorrelation to delineate the mid-lithosphere discontinuity beneath the North China Craton, and Sun et al. (2018) have used a similar approach to study multiple discontinuities in the West Australian Craton.

The *P* reflectivity extracted from autocorrelograms includes free-surface effects, and hence surface multiples. Such multiples are rarely any problem because the reflection coefficients at vertical incidence are typically well below 0.1; so surface multiples are at least ten times smaller than primary reflections. Thus the 10-70 s two-way-time interval that includes reflections from the Moho and the full span of the lithosphere is dominated by primary reflections, and so provides direct information on the nature of heterogeneity. The Moho appears as the base of crustal reflectivity. Reflections from below the Moho are generally of slightly lower frequency, but are distributed throughout the lithosphere for the 0.3-4 Hz frequency band.

For conventional reflection profiling using frequencies above 10 Hz, the upper part of the mantle is regarded as seismically transparent compared with the crust that shows distinct, and organised, reflectivity. Even when ultra-long reflection records have been collected, only a few discrete mantle reflectors have been recognised (Warner et al., 1996; Hammer et al., 2010). Yet, significant structure emerges with lower frequency illumination, indicating larger scale lengths than in the crust.

## 4. Spatial stacks and images along the BILBY profile

In Figure 2 we compare three different ways of investigating the structure beneath the BILBY line using results projected onto a NS profile along $134°E$. We use stacked autocorrelograms from continuous data that provide an estimate of apparent *P*-wave reflectivity beneath the stations, common reflection point stacking from autocorrelograms of teleseismic arrivals (ACS – see Appendix A.1), and common conversion point (CCP) stacks of receiver functions from Sippl (2016).

Yoshizawa and Kennett (2015) have pointed out that inflections in the radial anisotropy represented through $\xi = (V_{\rm sh}/V_{\rm sv})^2$ tie well to estimates of MLD depth from *Sp* receiver functions at permanent stations in Australia (Ford et al., 2010), including WRAB which lies on the profile, close to BL07. We therefore concentrate on this aspect of the large scale structure, which is used as a background in the upper panel of Figure 2. We display the stacked station autocorrelograms from continuous data, constructed as in Gorbatov et al. (2013), as two-sided variable density displays in a column beneath each station. Conversion from reflection time to depth has been made using a modified version of the global velocity model *ak135* (Kennett et al., 1995) with a crustal thickness of 45 km instead of 35 km. The top 15 km of the autocorrelograms are muted to avoid contamination from the large contributions at very small lags. Figure S1 in the Supplementary material shows the autocorrelogram traces directly, superimposed on the absolute *S* wavespeed profile as well as the radial anisotropy.

The stacked station autocorrelograms exploit the full continuous trace, so that they include information from both ambient noise and earthquake signals. This region of Central Australia receives noise from many different azimuths, and Kennett (2015) has shown the temporal consistency of the autocorrelograms at ASAR. The processing employed retains the natural balance of frequencies and uses high-pass filtering to suppress effects from the zero-time peak in the autocorrelation. In consequence, we are not able to push the lower frequency limit on the apparent *P*-wave reflectivity traces below 0.125 Hz. The North Australian Craton shows rather strong lithospheric scattering, so that there can be some contamination of the apparent *P*-wave reflectivity by late energy whose propagation path is not near vertical. The most noticeable effects are at the stations BL06, BL08, and BL15.

Along the BILBY profile the transition from crust to mantle is gradational (Sippl, 2016). As a result, crustal multiples are rather weak. Although this complicates standard methods using stacking to estimate crustal thickness, the weak multiples are very helpful for investigating lithospheric discontinuities using receiver functions.

The application of common conversion point (CCP) stacking to the results of individual receiver function traces from teleseismic arrivals is now a common practice. Sippl (2016) has demonstrated the effectiveness of CCP stacking for the BILBY profile as shown in the bottom panel of Figure 2. The focus in that work was on the topography of the Moho, but there are clear indications of structure at larger depth. In the Central Australian region the influence of crustal multiples is muted, so that deeper structures can be investigated. We introduce here an analogous approach to imaging deeper structure using the common reflection point stacking of autocorrelograms from teleseismic events. This approach uses the same portion of the teleseismic waveforms as exploited in receiver function studies. The autocorrelation of the transmitted *P* waves arriving at a station at the free surface provides a direct estimate of the *P* reflectivity for the incident slowness (Sun and Kennett, 2016b). As discussed in the Appendix, the locus of the reflection points lies on the propagation path for the first-arriving *P* wave. We can therefore map the autocorrelograms of immediate coda of the *P* arrivals onto this path as a function of time, and hence depth. The contributions from the different events and stations are stacked as a function of horizontal position and depth, to provide low-fold reflection imaging. Further details of the procedure are provided in Appendix A.1.

In the middle panel of Figure 2, we display the results of such reflection point imaging projected onto the 134°E profile. For stability we use a filter band peaking at 1 Hz, so that the frequency content in the reflection point imaging is a little lower than for the traces in the upper panel. We have used available events over a common period in time at all stations, so as to have as coherent a data set for imaging as possible.

In Figure S2 of the Supplementary Material, we make a comparison of the stacked station autocorrelogram results from continuous data in both the original frequency band (0.2-4.0 Hz) and in the reduced band (0.2-1.0 Hz) comparable to that used for the teleseismic imaging results displayed in Figure 2.

Both the common conversion point stack image and the reflection point image have been constructed using the same modified version of the *ak135* model with a thickened 45 km crust. In each case we have projected the results onto a north-south profile, but the actual distribution of the propagation paths forms a 3-D distribution around the line. The main areas of teleseismic seismicity lie to the north and east of the profile, with a particular concentration from the Tonga-Fiji subduction zone. This means that the projected image reflects an average of a zone around the profile along 134°E. In Figure 3 we show the piercing points at 100 km for the teleseismic $P$ waves used in constructing the reflection image. Most events come from the north and east, with a concentration associated with Tonga-Fiji events to the eastern side of the profile. The images in Figure 2 thus reflect an average over a band around the profile line 134°E.

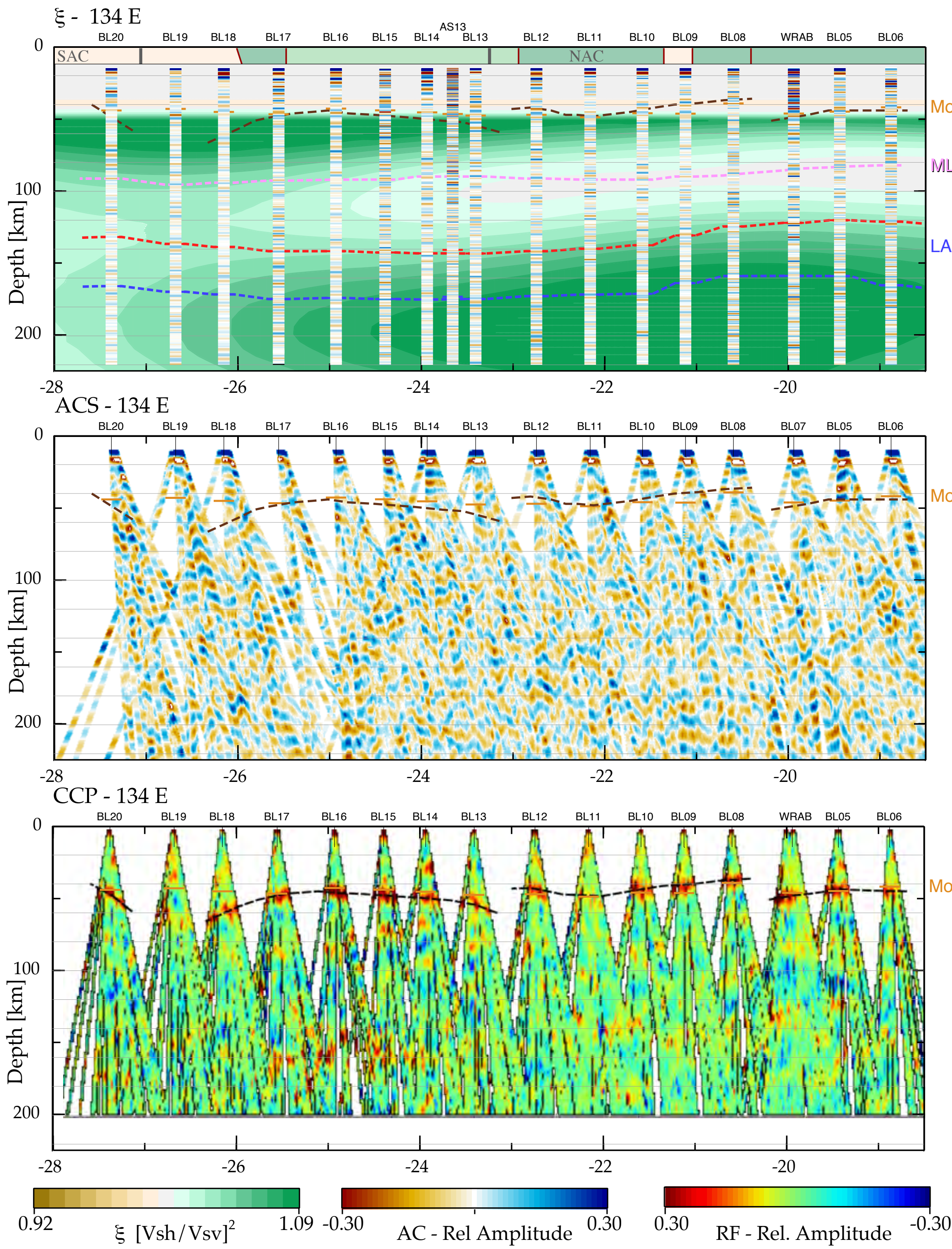

ξ - 134 E
BL20 BL19 BL18 BL17 BL16 BL15 BL14 AS13 BL13 BL12 BL11 BL10 BL09 BL08 WRAB BL05 BL06
SAC
NAC
Moho
MLD
LAT
Depth [km]
0
100
200
-28 -26 -24 -22 -20
ACS - 134 E
BL20 BL19 BL18 BL17 BL16 BL15 BL14 BL13 BL12 BL11 BL10 BL09 BL08 BL07 BL05 BL06
Moho
Depth [km]
CCP - 134 E
BL20 BL19 BL18 BL17 BL16 BL15 BL14 BL13 BL12 BL11 BL10 BL09 BL08 WRAB BL05 BL06
Moho
Depth [km]
0.92
ξ [Vsh/Vsv]²
1.09
-0.30
AC - Rel Amplitude
0.30
0.30
RF - Rel. Amplitude
-0.30

Figure 2: Comparison of stacked station autocorrelation results with reflection point stacking from teleseismic arrivals (ACS) and common conversion point stacking (CCP) of receiver functions projected onto a profile along 134°E. Two-sided variable area displays of the station autocorrelograms are plotted on top of the radial anisotropy from the model of Yoshizawa (2014). The light brown markers show the Moho depths from the smoothly interpolated model of Salmon et al. (2013). The pale purple markers indicate the depth picked for the mid-lithosphere discontinuity indicated by the change in frequency content of stacked autocorrelograms (MLD). The Moho profile from Sippl (2016) is shown on all panels. The red and blue markers in the top panel indicate the shallower and deeper bounds on the lithosphere-asthenosphere transition (LAT) at each station position (Yoshizawa, 2014). In the upper panel a summary strip of the tectonic environment along the profile is included, using the colour scheme of Figure 1(b). The approximate positions of the boundaries of the South Australian Craton (SAC) and North Australian Craton (NAC) are also marked.

The conversion points for the common conversion point stack results displayed in Figure 2, have a similar pattern to the P piercing points shown in Figure 3, but lie closer to the stations, because of the steeper paths of the converted *S* leg. This means that the sampling beneath stations in CCP stacking, using *Ps* receiver functions, covers a tighter zone around a station than for reflection stacking (ACS) using just P energy.

In the bottom panel of Figure 2, we show the common conversion point (CCP) stacks of receiver functions from Sippl (2016), projected onto the same N-S profile along 134°E. The autocorrelogram sections and the CCP results are plotted on the same scale for both horizontal position and depth. For the CCP stacks, the ray paths for the receiver functions from individual teleseisms are calculated using the same modified *ak135* model. The paths are then projected onto the 1200 km long N-S profile discretized into $2 \times 2$ km cells down to 200 km depth. The amplitudes of the individual receiver functions were mapped into these cells following the conversion ray paths. Finally, the amplitudes in each cell were summed and averaged, and are displayed as fractions of the *P* amplitude. We display on each panel the Moho

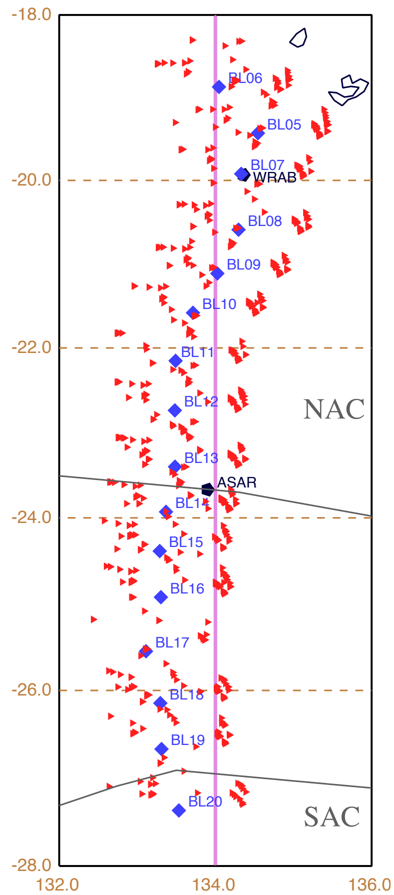


Figure 3: Piercing points at 100 km depth for teleseismic *P* waves used in the construction of the reflection point images shown in Figure 2. The station locations and craton boundaries are indicated, along with the line of section at 134°E. SAC – South Australian Craton; NAC – North Australian Craton.

picks made by Sippl (2016) that tie well to the base of crustal *P* reflectivity from the autocorrelogram results.

In the depth range from 80-100 km depth at most of the BILBY stations there is a distinct change in the frequency content of the apparent *P*-wave reflectivity. Initial visual picks were confirmed using instantaneous frequency analysis, and the trajectory of these indicators of a mid-lithospheric discontinuity are shown as a dashed mauve line in the upper panel of Figure 2. Instantaneous frequency results for the stacked autocorrelograms for the BILBY experiment are displayed in the Supplementary Material to Kennett et al. (2017). Two of the most distinct indicators of a potential MLD are for stations at the two arrays on the line, and these will be considered in detail in the next section.

On the station autocorrelogram traces we also show the shallower and deeper bounds on the extent of the lithosphere-asthenosphere transition (LAT) from Yoshizawa (2014). The shallow bound on the LAT is taken at the maximum negative gradient of *S* wavespeed, and the deeper bound at the minimum absolute *S* wavespeed. Thus, both bounds lie in a zone where shear velocity is decreasing with depth. The shallower bound commonly lies just below the highest absolute *S* wavespeed.

Neither the CCP stacks nor the reflection point imaging show the presence of strong lithospheric discontinuity signals. But there are some subtle indicators of contrast, such as a change in the character of the CCP traces close to the depth suggested for an MLD. Typically this is associated with a modestly negative amplitude feature. The situation is more complex for the station group BL16–BL13 that is also sampled by the Alice Springs Array (ASAR).

On the autocorrelogram traces we commonly see a slight change in the character of the reflectivity in the depth range spanned by the bounds on the LAT. A similar feature is present on the CCP stacks with noticeable conversion occurring close to the shallower bound on the LAT, particularly at the northern end of the profile.

### *4.1. Continuity of lithospheric discontinuities across arrays*

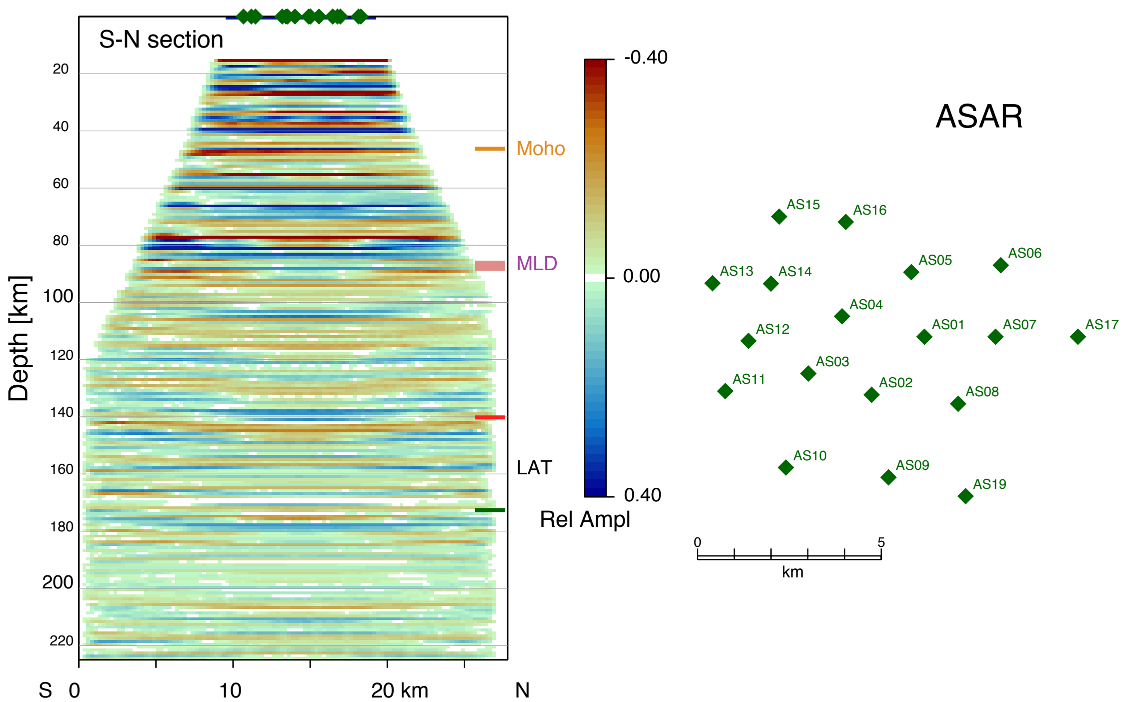


Figure 4: Migrated station autocorrelation results for the short-period stations of Alice Springs array (ASAR) projected onto a north-south profile. The configuration of the array is displayed in the right panel.

The BILBY profile provides an unusual opportunity to look at the continuity of lithospheric features at different scales, using the dense permanent arrays that abut the line. Kennett (2015) has pointed out the good coherence in the general features of the autocorrelograms across the short-period stations of the Alice Springs array (ASAR). Here we look more closely at the character of the prominent discontinuity at around 88 km depth, and the nature of the LAT (Figure 4). The original autocorrelogram traces are displayed in Figure S3 of the Supplementary Materials in a south-north section.

We have used the Kirchhoff migration approach of Ito et al. (2012) to combine the stacked autocorrelation results, from continuous seismic records, for all the ASAR array stations on a north-south profile. This allows us to give an indication of the lateral continuity of reflectivity features. This procedure traces back possible ray paths using the same velocity model as employed in the reflection point and common-conversion point stacks. We describe our implementation of this approach in Appendix A.2. The resulting migrated reflectivity section is displayed in Figure 4

In Figure 4 we see consistent crustal reflectivity across the span of the ASAR array with a modest terminal reflection doublet to mark the base of the crust. Lateral continuity in the P-wave reflectivity across the ASAR array remains strong at greater depth, with features extending over about 15 km horizontally. A strong burst of reflectivity occurs at around 80 km depth, with consistency on the NS profile; indeed similar continuity is seen on an EW projection. There is a distinct base to this reflectivity at around 88 km. Lower amplitude reflectivity across the profile is seen above 76 km and below 88 km. Just below 100 km depth a distinct reflector emerges across the central part of the array. Close to 140 km, near the shallower bound on the LAT from Yoshizawa (2014), we note a rise in the level of reflectivity, which continues to greater time (depth). A similar increase in reflectivity occurs just below the deeper bound on the LAT.

The prominent mid-lithospheric feature at ASAR occurs in a region where *Pn* tomography (Sun and Kennett, 2016a) indicates a zone of lowered *P* wavespeed in the uppermost mantle extending to around 75 km depth, below thickened crust. There is then a hint of a *P* wavespeed reduction below 90 km, but this is not well resolved. Certainly both the *Pn* results and the character of the reflectivity suggest

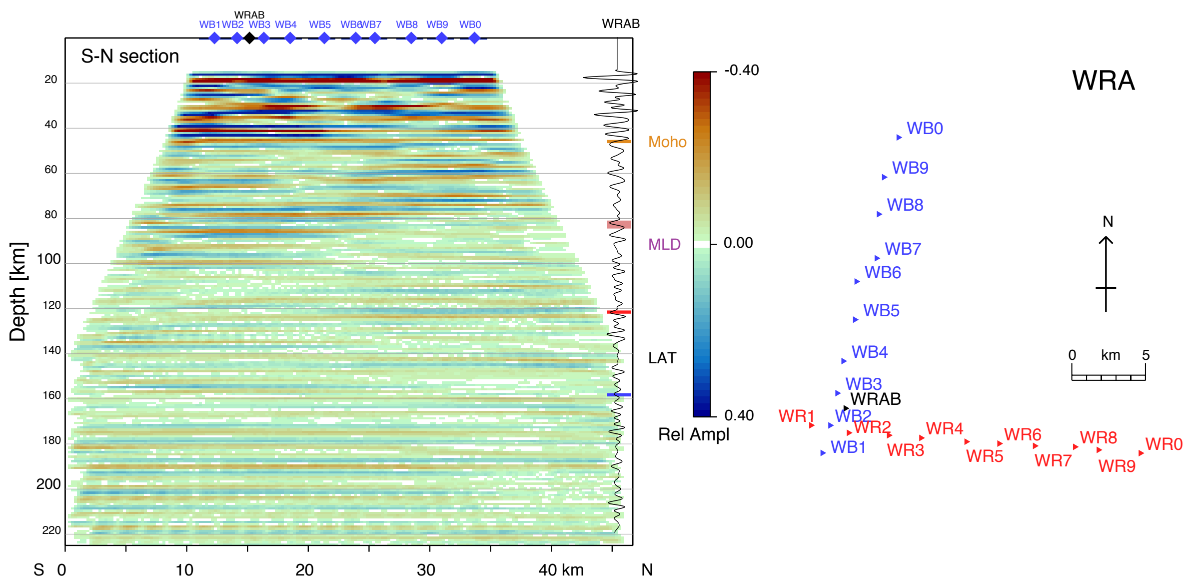


Figure 5: Migrated station autocorrelation results for the broad-band stations of the Warramunga array (WRA) and the station WRAB projected onto profiles along the array arms. The configuration of the array is displayed in the right panel. The purple marker at station WRAB indicates the mid-lithospheric discontinuity depth inferred by Ford et al. (2010) from *Sp* receiver functions.

that a distinct mid-lithospheric change extends across the full area of ASAR. The tie to the nearest stations on the BILBY profile, BL13 and BL14, is fairly good, particularly when we recognise the different (broad-band) instrumentation.

The Warramunga array (WRA) lies very close to station BL07 on the main profile. This L-shaped array has broad-band vertical component sensors at all sites, and the WRAB station lies close to the crossing point of the two arms (Figure 5). We again display a Kirchhoff migration of the autocorrelogram traces projected onto a north-south profile using the WB stations from the NS arm. To the right we display the stacked autocorrelogram trace for WRAB on which we mark the estimated MLD depth from the work of Ford et al. (2010) using *Sp* receiver functions at much lower frequencies. The full suite of autocorrelogram traces for both arms of the array are displayed in Figure S4 of the Supplementary Material.

The migrated autocorrelograms at WRA in Figure 5 show more horizontal variability than at ASAR, even allowing for the larger aperture of the array. We see a clear evolution of crustal structure along the profile, though the base of the crust is at a nearly constant depth. There is also a distinct change in style of reflectivity between the southern and northern zones in the uppermost mantle, with a shift of reflectivity to shallow levels in the north. A band of reflectivity occurs around the 81 km depth of the MLD of Ford et al. (2010) at WRAB in the south. For the frequencies used in the *Sp* receiver function analysis, all of this group of reflections would coalesce. Weak reflectivity occurs near the shallower bound on the LAT across the full profile.

The patterns of behaviour seen in Figure 5 are consistent with the presence of horizontal scale lengths of the order of 10-15 km in the upper part of the lithospheric mantle. This result ties well with the multi-scale heterogeneity model discussed by Kennett et al. (2017). In the LAT zone, the multi-scale model includes a smaller horizontal scale length for fine structure, as previously suggested by Thybo (2006). The migration at this depth tends to smear significantly in the horizontal direction, so it is hard to gauge whether there is any change. In Figure 8 we present synthetic migrated results from the multi-scale heterogeneity model of Kennett et al. (2017) that display similar behaviour to the array observations.

### 4.2. *Tracking lithospheric features*

The 10-15 km horizontal correlation length seen at the two arrays can help to explain the difficulty in tracking consistent features across the BILBY profile. The $\sim$50 km separation of the stations is too large to allow continuity of features when seen at higher frequencies.

In Figure 6 we transfer the trajectory of the individual station picks for the

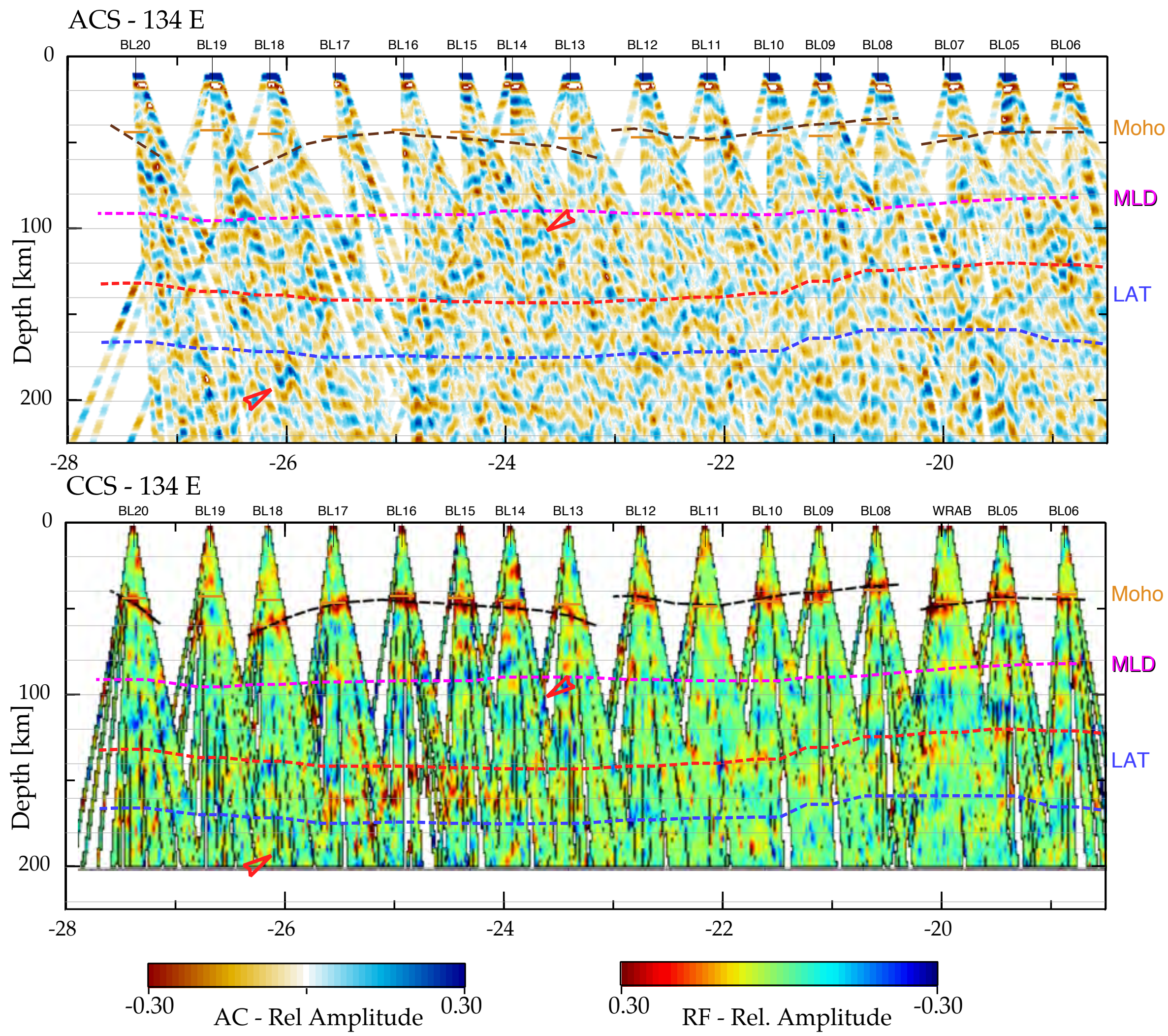


Figure 6: Comparison of reflection point stacking from teleseismic arrivals (ACS) with common conversion point stacking of receiver functions (CCS), projected on to a profile along 134°E. The Moho, MLD, and bounds on the LAT are marked as in Figure 2. The dipping feature is indicated with a red marker.

MLD on to the CCP and ACS plots as a purple dashed line. We also show the shallower and deeper bounds on the LAT as red and blue dashed lines. With the aid of these guidelines, we can see some hints of changes in reflectivity in the neighbourhood of the MLD. In both the ACS reflection stack and CCP images we see a tendency for enhanced reflectivity in the LAT zone, with a patchy association of features at the shallower bound. In Figure S5 of the Supplementary Material, we present an alternative display of the reflection stack exploiting the derivative of the original. This operation enhances the shallow reflectivity relative to the deeper and so makes some features more visible.

The ACS images provide a low-fold rendering of the reflection response along the profile. The record section in the upper panel of Figure 6 is complex with a considerable variety of behaviour. We concentrate attention on features that show the greatest horizontal continuity, since this is unlikely to occur by chance.

Of particular interest in Figure 6 is the indication of a distinctive dipping horizon descending from around 90 km depth at station BL13 to close to 200 km at station BL18 (26°S) – indicated by red markers. To the north of BL13 this horizon appears to sole out at around 75 km and link to reflectivity that stops at the MLD.

The presence of this dipping feature is indeed unexpected, since the last postulated subduction event in this area was at around 1900 Ma (Korsch et al., 1998). We speculate that this feature could represent a large-scale dipping shear zone that acted as a detachment surface in the compression associated with the Petermann and Alice-Springs Orogenies.

There is a strong correspondence between the structures imaged with the reflection point approach and the common conversion point stacks, as illustrated in Figure 6. As noted above, the fan of arrivals with converted waves is tighter, so significant overlap between results from different stations only occurs below 100 km. The dipping feature seen in the upper reflection point image can be tracked in the lower panel of CCS stacks, once one knows where to look. Though the strongest expression is at slightly shallower depth than in the reflection stack. In both images the horizontal extent of distinct features rarely reaches 100 km horizontally. Indeed there is a general resemblance to the character of crustal seismic reflection data on a much expanded scale in space and time (cf. Kennett and Saygin, 2015). When fine scale structures are present, reflections arise from complex interference phenomena, and so rarely emulate simple interfaces.

The CCP results depend on conversion from P to S waves, whereas the autocorrelation stacks utilise P reflections, with a different sensitivity to structure. In particular the effect of dipping structures will be different in the two cases. The orientation of the main southern dipping feature relative to the available sources is less favourable for conversion, which explains the weaker signal. Also, contamination by surface multiples is more likely in the CCS image than the ACS.

## 5. Nature of the lithosphere beneath Central Australia in a global context

Receiver function studies in continental areas around the world have shown the presence of a near-ubiquitous negative phase, indicative of a velocity decrease with depth, about 70-110 km beneath the surface. This feature was initially interpreted as the lithosphere-asthenosphere boundary (e.g. Bostock, 1998; Rychert and Shearer, 2009). However, it soon became apparent that this explanation is clearly inconsistent with S-wavespeeds from global and regional models in the case of old, cratonic regions, which possess pervasive fast mantle lithospheric ‘keels’ extending to $\geq$200 km depth (e.g. Becker and Boschi, 2002). Thus the apparent velocity decrease inside the mantle lithosphere, which had already been identified in active seismic data (Thybo and Perchuc, 1997), was termed the mid-lithospheric discontinuity or MLD (e.g. Abt et al., 2010; Fischer et al., 2010).

While earlier studies investigating *Sp* receiver functions filtered to long periods generally obtained a single, clear negative MLD phase, a number of recent studies of *Ps* receiver functions or higher-frequency *Sp* receiver functions have observed a much more complex nature of the MLD beneath the North American and African cratons (e.g. Lekić and Fischer, 2014; Wirth and Long, 2014; Cooper and Miller, 2014; Hopper et al., 2014; Chen et al., 2018). Instead of a single, discrete velocity discontinuity, it appears as if a depth 'corridor' containing several negative phases (Wirth and Long, 2014) or even both negative and positive phases (Selway et al., 2015) emerges when higher frequencies are considered. Filtering to long periods then merges these complex features into a single negative phase. Even a number of studies operating at relatively low frequencies have obtained multiple MLDs (Sodoudi et al., 2013; Calò et al., 2016).

For the Australian continent, an MLD has been observed for the Archean and Proterozoic western two thirds of the continent (Ford et al., 2010; Sun et al., 2018). The work of Sun et al. (2018) uses stacked autocorrelations of teleseismic *P* arrivals at stations in Western Australia, and finds a rather shallow MLD at 62-82 km across the West Australian Craton, and indications of a second feature at depths in the range 100-120 km, near the shallower bound on the LAT.

The Ford et al. (2010) work with permanent stations across Australia uses *Sp* receiver functions at relatively low frequency. The frequencies employed in both Sippl (2016) and the present study are significantly higher, thus it is unsurprising that our results show a more heterogeneous and complex picture. For station WRAB, Ford et al. (2010) observed an MLD at 81$\pm$14 km depth, as well as a deeper positive phase at depths of $\sim$150-180 km. We find throughout the depth range of 60-100 km predominantly negative phases in the *Ps* receiver functions, and a banded weak reflectivity structure in the autocorrelations (Figures 2 and 6). It is interesting to note that this 'MLD' depth zone is associated with a distinct change in anisotropy (Figure 2). It is currently unclear what causes the MLD, but a change in anisotropy signature with depth is one of the candidate physical mechanisms (Selway et al., 2015), and some recent studies in the central US have indeed observed the co-location of an anisotropy switch with the MLD depth range (e.g. Wirth and Long, 2014).

The positive phase at $\sim$150-180 km depth for station WRAB in Ford et al. (2010) appears to correlate with a depth region of predominantly positive amplitudes in the *Ps* receiver functions of Sippl (2016), as shown in Figures 2 and 6. Since Ford et al. (2010) employed *Sp* receiver functions, this coincidence excludes the possibility that these features in the *Ps* receiver functions are Moho multiples. In the autocorrelations, we observed an increase in reflectivity for some stations in this depth corridor, which also features a strong anisotropy gradient. Commonly, positive receiver function phases in this depth range are often not interpreted or simply considered to be a consequence of general complexity.

Finally, we do not note any clear negative phases that could represent the lithosphere-asthenosphere boundary (LAB) in the Central Australian region. Although a number of global studies have identified an LAB as a separate phase beneath the MLD in areas of thick lithosphere (e.g. Sodoudi et al., 2013), most available published evidence hints at the absence of such a deeper RF phase where an MLD is observed. Abt et al. (2010) interpreted this observation as the LAB being a purely thermal boundary in regions of thick lithosphere, which would lead to a very gradual velocity decrease spread over a vertical distance of $\geq$50 km, thus subtle enough to not produce a clear anomaly even in low-frequency *Sp* receiver functions. Under Central Australia, we observe a slight decrease in P wave reflectivity, similar to the one at MLD depth, in the vicinity of the lower bound on the LAT from Yoshizawa (2014).

In summary, we note that we do not retrieve any clear, distinct phases that can be associated with either MLD or LAB. However, when interpreting the subtle, sometimes laterally discontinuous, observations together with high-frequency *Ps* receiver functions and anisotropy, a picture emerges of a highly complex lithospheric architecture, perhaps better characterized by volumes of subtle velocity and reflectivity gradients than by the assumption of sharp discontinuities. This concept is in agreement with recent observations from other cratonic areas around the world (e.g. Lekić and Fischer, 2014; Wirth and Long, 2014), and the multi-scale cratonic heterogeneity model of Kennett et al. (2017),

## 6. Discussion

The BILBY profile crosses a complex cratonic suture zone with an extended history of deformation. Though there have been no major orogenic events since 300 Ma, north-south deformation associated with the plate boundary collision in New Guinea is manifested in neotectonic activity, with three Mw 6+ events within 12 hours near Tennant Creek in 1988 (Bowman, 1992), and a further sequence of Mw 5+ events in Central Australia in recent years (e.g., Clark et al., 2014).

There is significant variation in crustal thickness along the BILBY profile with distinct Moho jumps indicative of the past deformation (e.g., Sippl, 2016). Despite this, images of full lithospheric structure provide little hint of prior tectonic events, with strong continuity of structure below 100 km depth and high shear wavespeeds (Fishwick and Reading, 2008; Kennett and Iaffaldano, 2013; Yoshizawa, 2014). As illustrated in Figure S1 of the Supplementary Material, high velocities extend deep and the lithosphere-asthenosphere transition with decreasing *S* wavespeeds is typically less than 50 km thick. *Pn* tomography (Sun and Kennett, 2016a) indicates contrasts below the relatively thick crust, with lowered velocities in the uppermost mantle down to 80 km, notably near Alice Springs (ASAR).

In the various receiver based studies, a feature near 90 km depth occurs along much of the BILBY profile, with a distinct high-frequency expression that ties well to the *Sp* receiver function results at WRAB at much lower frequencies (Ford et al., 2010).

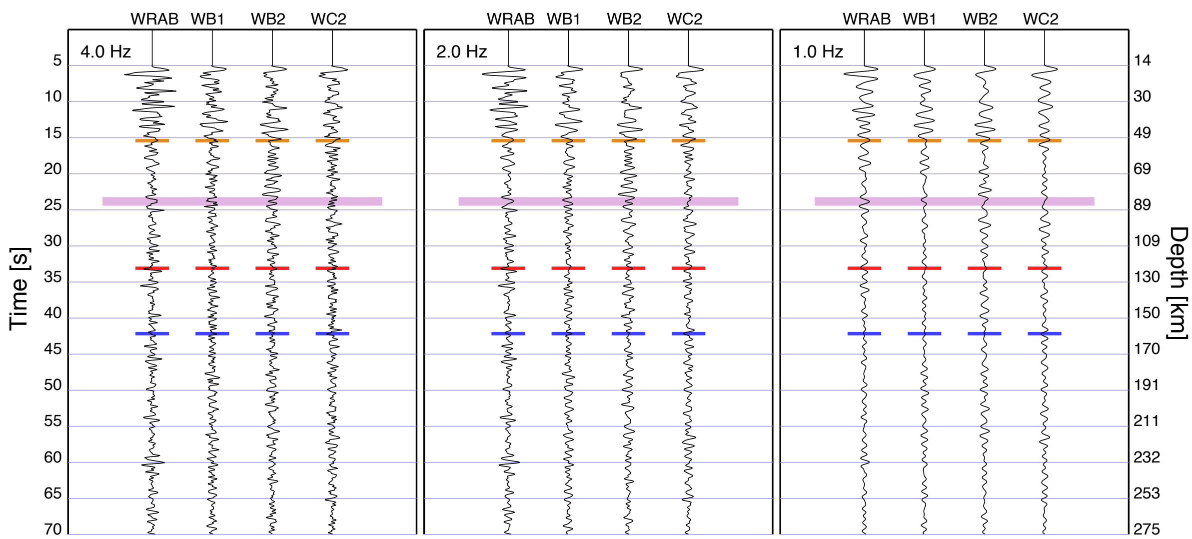


Figure 7: Frequency dependence of apparent *P*- wave reflectivity for the group of stations near WRAB. The band-pass filters have a common lower corner frequency of 0.125 Hz and upper corner of 4.0 H, 2.0 Hz, and 1.0 Hz as indicated in the upper left corner of each panel. The Moho and the bounds on the LAT are marked as in Figure 2 together with an indicator of the MLD suggested by Ford et al. (2010).

In Figure 7 we compare the character of the apparent *P*-wave reflectivity at the group of stations closest to WRAB as a function of the upper corner frequency, with a common lower limit of 0.125 Hz. WRAB is a borehole station and the other three shallowly emplaced vertical broad-band sensors. As the upper frequency corner diminishes the visibility of the distinctive features close to 90 km reduces, and is hard to discern for frequencies below 1 Hz. The strong frequency dependence of the reflection packet suggests that the apparent MLD arises from wave interference from fine-scale variations in the lithosphere modulating larger-scale structure as proposed by Kennett and Furumura (2016) and Kennett et al. (2017). Variations in fine-scale structure can have the effect of changing the apparent radial anisotropy.

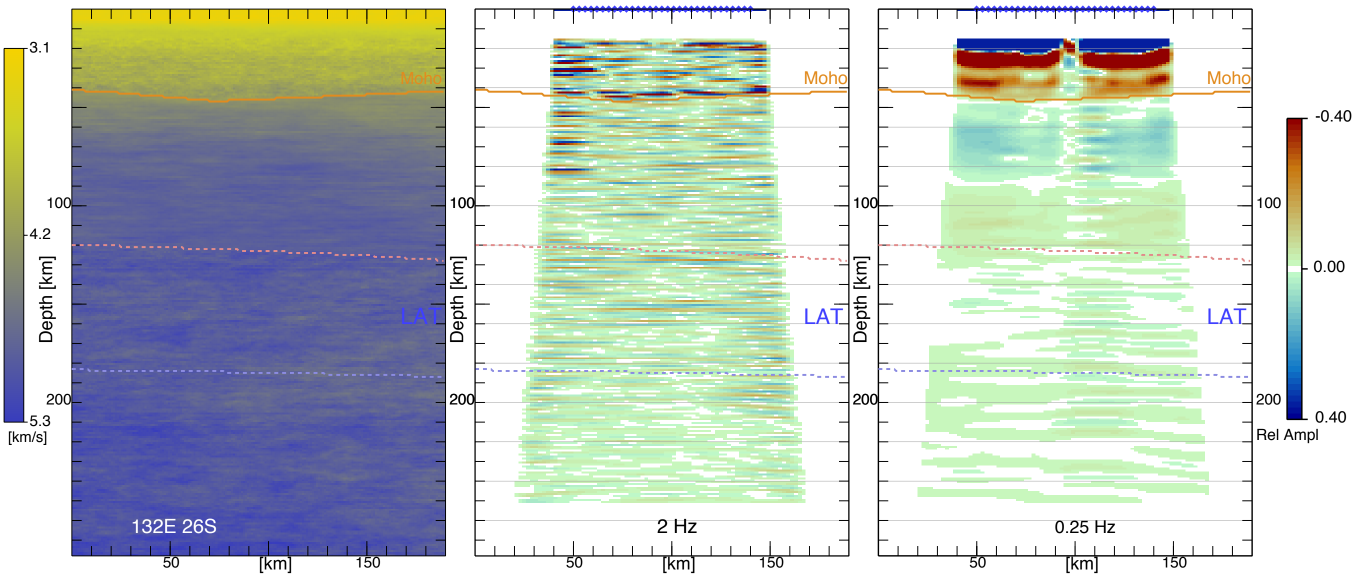


Figure 8: Segment of the multi-scale heterogeneity model of Kennett and Furumura (2016) for the region around 26°S along 132°E represented in terms of shear wavespeed, accompanied by migrated results for a 90 km aperture array with 3 km station spacing constructed as in Figures 4 and 5 but now using synthetic autocorrelograms stacked over a range of slownesses at each station. Results are shown for an upper filter corner of 2 Hz and 0.25 Hz. All images are approximately true scale.

The multi-scale model of Kennett and Furumura (2016) includes significant variation in the crust with larger amplitudes between 15 km depth and the Moho. The lithospheric mantle is mildly heterogeneous with longer horizontal correlation lengths, which are needed to produce the minutes of coda duration for both *P* and *S* waves for passage through the Precambrian zones. Between the bounds on the LAT extracted from the model of Yoshizawa (2014) a change in heterogeneity regime is imposed with larger amplitude and shorter horizontal correlation length (cf.

Thybo, 2006). This composite model with many different scales of heterogeneity in various depth ranges gives rise to a rich structure with a slow decline in the wavelength spectrum (Kennett and Furumura, 2016, Figure 4).

In the left hand panel of Figure 8 we illustrate a segment from a 2-D realisation of this multi-scale model. We show the shear wavespeed variations for a small zone around 26°S on a profile along 132°E, and thus close to the southern part of the BILBY profile. From this 2-D model we have constructed synthetic autocorrelograms for a suite of stations at 3 km intervals with stacking over a range of incident slownesses, as in Kennett and Furumura (2016). We have then used the migration procedure employed for the ASAR and WRA arrays in Figures 4 and 5 to produce reflectivity images of the subsurface from the 90 km long array of stations.

The central panel of Figure 8 show the migration results with an upper corner frequency of 2 Hz, and the right hand panel with an upper corner frequency of 0.25 Hz. The multi-scale structure produces a complex pattern of P wave reflectivity at higher frequencies that both reproduces the variations of the wavespeed distribution and has a strong resemblance to the observations at the permanent arrays, although deep reflectivity is a little stronger in the synthetic results. As noted by Kennett et al. (2017) reducing the corner frequency produces an apparently simple result although the underlying model is unchanged. We see visible changes at the Moho, at around 80 km depth (an apparent MLD?), and at the top of the lithosphere-asthenosphere transition. Such features are present in the central panel but not as distinctive. The synthetic reflectivity patterns recover the scale lengths of the input model in the shallower part of the section with some horizontal elongation, but below 100 km the smearing effects are stronger and one would not recognise the 5 km horizontal correlation length of the original model.

This synthetic test demonstrates both the potential of the autocorrelogram results for imaging structure, and the complex effects of wave interference in a model with fine-scale features modulated by longer wavelength components.

## 7. Conclusions

We have been able to demonstrate the effective use of autocorrelations of teleseismic *P*-wave arrivals as an imaging tool, that ties well with prior common conversion point (CCP) results. Both methods reveal the presence of a hitherto unsuspected south-dipping reflector under the cratonic suture zone that most likely represents the former mantle detachment zone associated with the Alice Springs orogeny.

The imaging results with both *P* reflectivity and conversions are consistent, and indicate a change in lithospheric properties around the depth of the shallower LAT bound of Yoshizawa (2014). The deeper LAT bound at the minimum absolute *S* wavespeed does not have any distinctive association in the images. There is no strong manifestation of a shallower MLD around 90 km in either of the imaging methods, though tentative correlations can be made at a number of stations. This is not surprising given the limited span of spatial correlation (10-15 km) seen across the permanent arrays.

Lithospheric discontinuities undoubtedly occur on a range of spatial scales. With a profile of moderately close stations we have been able to track a high-frequency change near 90 km depth from changes in apparent *P*-wave reflectivity, that appears to have an association with reductions in radial anisotropy. With slightly lower frequency imaging methods using either direct or converted waves the strongest correlations occur with the top of the velocity reduction leading into the transition from lithosphere to asthenosphere.

Despite local agreement on MLD depth, it remains hard to link observations of mid-lithospheric discontinuities at different frequencies. A likely cause of higher-frequency behaviour comes from the influences of a change in fine structure that manifests as a change in wave interference pattern. As the frequency reduces, the overlap of the different interfering phases is such as to remove a distinct change in frequency, but instead form a broader pulse that might be interpreted as the expression of a jump in material properties (Kennett et al., 2017). Simplified models may then be misleading as to appropriate contrast in physical properties.

## Acknowledgements

Data for the permanent stations and some early portable stations from Australia is available from the IRIS Data Management Service in Seattle, the remaining data for portable stations is held in the archive at the Research School of Earth Sciences, Australian National University.

We would like to thank the RSES staff, led by Sarah Pozgay, who conducted the BILBY experiment under often trying conditions, and also Elizabeth Vanacore who carried out early analysis of the data. Discussions with Benoît Tauzin on imaging using autocorrelation results are gratefully acknowledged.

## A. Appendix

### *A.1. Common reflection point imaging with autocorrelograms of teleseismic P*

In a similar way to the common conversion point stacking used for receiver functions for incident P waves (e.g., Dueker and Sheehan, 1997; Zhu, 2000; Wittlinger et al., 2004) we can develop images of the sub-surface by combining and stacking results from teleseismic autocorrelation at many stations. We exploit the coincidence of the reflection points for incoming P waves with the ray trajectory of the first P arrival (Figure A1). The approach is based on the arrival of a plane wave with a well-defined slowness from teleseismic distances, and a slowly varying structure. The points at the surface where the transmitted waves arrive can be viewed as a set of virtual sources generating the reflected waves that arrive at the station.

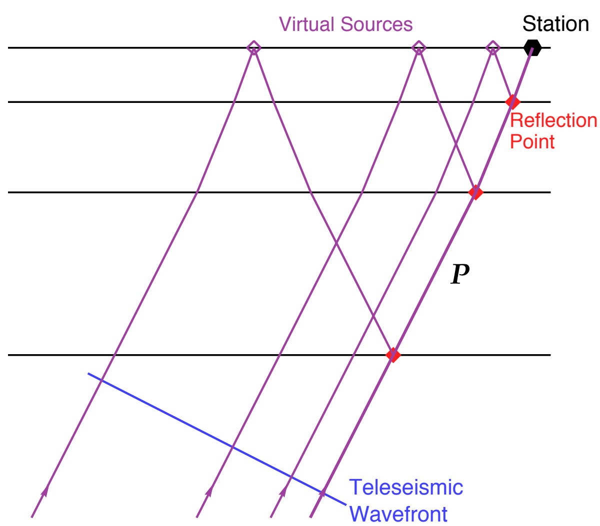


Figure A1: Reflections from the surface for transmitted *P* waves provide virtual sources for reflection from depth. The trajectory of the reflection points follow the *P* ray path.

The scheme we have implemented is based on the development made by Tauzin et al. (2016), but adapted to P wave reflection rather than P to S conversion. The region beneath the profile is discretized in both horizontal position and depth and we then accumulate all the contributions from the suite of stations for the full suite of teleseismic arrivals to produce a common reflection point stack.

For each event at a particular station, we compute the P wave ray path for the incident slowness and map the autocorrelation function from the teleseismic coda onto the path converting two-way reflection time to depth, so that the reflections are mapped onto the cells. We also apply smoothing around the ray path to allow for the effects of finite frequency. We illustrate the mapping in Figure A.2 with the projection of the events recorded at station BL05 on to the South-north profile.

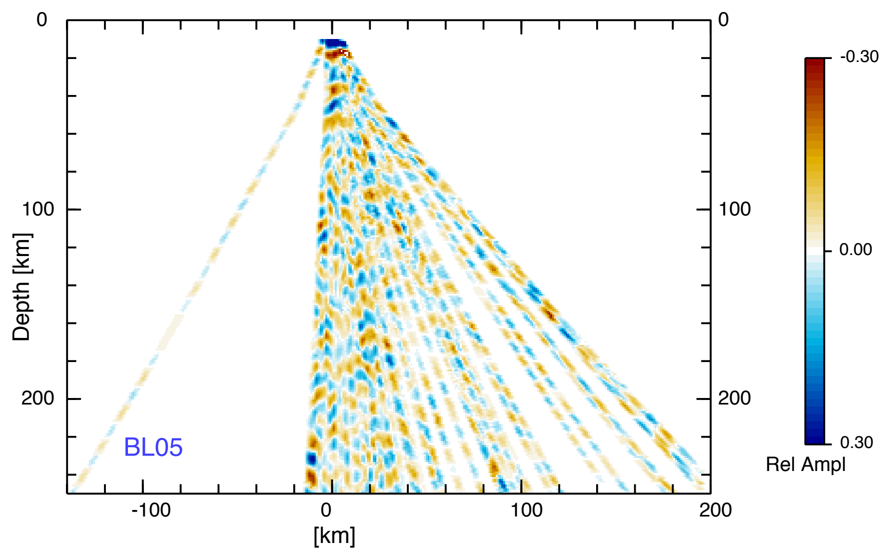


Figure A2: Mapping of the autocorrelation of teleseismic events recorded at station BL05 onto a south-north profile. Each event trace is mapped from time to depth following the ray path for its incident slowness in the *ak135* model, modified to include a 45 km thick crust.

As we add events and stations, we add further reflection point contributions to the various cells and stack, with normalisation by the number of hits on the cells. This autocorrelation stack (ACS) then maps out the apparent P-reflectivity along the profile as a function of position and depth.

Because deeper reflection points correspond to virtual sources further away from the receiver, lateral heterogeneity around the station will have an increasing influence with depth. The impact of such heterogeneity will be larger than for CCP stacks where just the transmission of the converted S wave is affected.

For the BILBY profile we use ray-tracing through the same modified version of the *ak135* model, with 45 km thick crust, as used in the CCP stacks. We represent the model with $1 \times 1$ km cells along the full profile and project each path with a 9 km wide tapered window, to allow for the sampling zone for frequencies around 1 Hz. The window is flat over the central 5 km and gaussian tapered at each end. The autocorrelogram results for each event-station pair are mapped from time onto the cells using ray-tracing for the appropriate incident slowness. All paths are projected onto the north-south section of the profile. The full suite of contributions in each cell is then stacked to produce the reflection point images displayed in Figures 2 and 6 with the label ACS.

### *A.2. Kirchhoff Migration for zero-offset traces*

Ito et al. (2012) introduced a form of Kirchhoff migration for station stacks of autocorrelograms for ambient noise, which we have adapted for use with our results using continuous seismic waveforms. The stacked autocorrelograms at each station are built up from contributions from a range of slowness from beneath the station, though they appear as a single trace equivalent to a zero-offset seismic reflection record. In the migration process we allow for a broadening range of sampling with depth beneath each station by mapping each station trace onto a suite of trajectories for a range of slownesses, with conversion of time to depth. We then stack all the migrated contributions from all the stations to provide an image of the reflection structure beneath an array. The results are best constrained over the central span of the stations where many station contributions overlap. The quality of the results diminish at the edges, because only one or two stations contribute.

We have used a discretization with cells 0.5 km wide and 1 km deep for the ASAR and WRA migrations shown in Figures 4 and 5. A wider cell with 2 km width is used for the migration of the synthetic autocorrelograms in Figure 8.

## References


Abt, D.L., Fischer, K.M., French, S.W., Ford, H.A., Yuan, H., Romanowicz, B., 2010. North American lithospheric discontinuity structure imaged by Ps and Sp receiver functions. J. Geophys. Res. 115, B09301. doi: 10.1029/2009jb006914.

Becker, T.W., Boschi, L., 2002. A comparison of tomographic and geodynamic mantle models. Geochem. Geophys. Geosyst. 3, 1003.

Bostock, M.G., 1998. Mantle stratigraphy and evolution of the Slave province. J. Geophys. Res. Solid Earth 103, 21 183–21 200.

Bowman, J.R., 1992. The 1988 Tennant Creek, Northern Territory, earthquakes: A synthesis Austr. J. Earth Sci. 39(5), 651–669.

Calò, M., Bodin, T., Romanowicz, B., 2016. Layered structure in the upper mantle across North America from joint inversion of long and short period seismic data. Earth Planet. Sci. Lett. 449, 164–175.

Chen, L., Jiang, M.M., Yang, J.H., Wei, Z.G., Liu, C.Z., Ling, Y., 2014. Presence of an intra-lithospheric discontinuity in the central and western North China Craton: Implications for destruction of the craton, Geology 42, 223–226.

Chen, C., Gilbert H., Fischer, K.M., Andronicos, C.L., Pavlis, G.L., Hamburger, M.W., Marshak, S., Larson, L., Yang, X. 2018. Lithospheric discontinuities beneath the U.S. Midcontinent - signatures of Proterozoic terrane accretion and failed rifting, *Earth Planet. Sci. Lett.*, 481, 223–235.

Clark, D.J., McPherson, A., Trevor, A., De Kool, M., 2014. Coseismic surface deformation caused by the 23 March 2012 Mw 5.4 Ernabella (Pukatja) earthquake, central Australia: Implications for fault scaling relations in cratonic settings Bull. Seismol. Soc. Am. 104(1), 24–39.

Cooper, C.M., Miller, M.S., 2014. Craton formation: Internal structure inherited from closing of the early oceans. Lithosphere 6, 35–42.

Direen, N.G., Crawford, A J., 2003. The Tasman Line: where is it, what is it, and is it Australia's Rodinian breakup boundary? Austral. J. Earth Sci. 50, 491–502.

Dueker, K.G., Sheehan, A.F., 1997. Mantle discontinuity structure from midpoint stacks of converted P to S waves across the Yellowstone hotspot track J. Geophys. Res. 102, 8313–8327

Fischer, K.M., Ford, H., Abt, D.L., Rychert, C.A., 2010. The Lithosphere-Asthenosphere Boundary. Ann. Rev. Earth Planet. Sci. 38, 551–575.

Fishwick, S., Reading, A.M., 2008. Anomalous lithosphere beneath the Proterozoic of western and central Australia: a record of continental collision and intraplate deformation? Precambrian Research 166, 111–121.

Ford, H.A., Fischer, K.M., Abt, D.L., Rychert, C.A., Elkins-Tanton, L.T., 2010. The lithosphere-asthenosphere boundary and cratonic lithospheric layering beneath Australia from Sp wave imaging. Earth Planet. Sci. Lett. 300, 299–310.

Gorbatov, A., Saygin, E., Kennett, B.L.N., 2013. Crustal properties from seismic station autocorrelograms. Geophys. J. Int. 192, 861–870.

Hammer, P.T.C., Clowes, R.M., Cook, F.A., van der Velden, A.J., Vasudevan, K., 2010. The Lithoprobe trans-continental lithospheric cross sections: imaging the internal structure of the North American continent. Canadian J. Earth Sci. 47, 821–857,

Hopper, E., Ford, H.A., Fischer, K.M., Lekić, V., Fouch, M.J., 2014. The lithosphere-asthenosphere boundary and the tectonic and magmatic history of the northwestern United States. Earth Planet. Sci. Lett. 402, 69–81.

Ito, Y., Shiomi, K., Nakajima, J., Hino R. 2012. Autocorrelation analysis of ambient noise in northeastern Japan subduction zone, Tectonophysics, 572573, 38–46.

Kennett, B.L.N., Engdahl, E.R., Buland, R., 1995. Constraints on seismic velocities in the Earth from travel times, Geophys. J. Int. 122, 108–124.

Kennett, B.L.N., Iaffaldano, G., 2013. Role of lithosphere in intra-continental deformation: Central Australia, Gondwana Res. 24, 958–968.

Kennett, B.L.N., 2015. Lithosphere-asthenosphere P-wave reflectivity across Australia, Earth Planet. Sci. Lett. 431, 225–235.

Kennett, B.L.N., Saygin, E., 2015. The nature of the Moho in Australia from reflection profiling: A review. GeoResJ 5, 74–91.

Kennett, B.L.N., Saygin, E., Salmon, M., 2015. Stacking autocorrelograms to map Moho depth with high spatial resolution in southeastern Australia, Geophys. Res. Lett. 42, 3839-3846.

Kennett, B.L.N., Furumura, T., 2016. Multiscale seismic heterogeneity in the continental lithosphere, Geochem. Geophys. Geosyst. 17, 791–809.

Kennett, B.L.N., Yoshizawa, K., Furumura, T., 2017. Interactions of multi-scale heterogeneity: Australia. Tectonophysics 717, 193–213.

Korsch, R., Goleby, B., Leven, J., Drummond, B.J., 1998. Crustal architecture of central Australia based on deep seismic reflection profiling. Tectonophysics 288, 57–69.

Korsch R.J. and Doublier M.P., 2016. Major crustal boundaries of Australia, and their significance in mineral systems targeting, Ore Geology Reviews 76, 211–218.

Lekić, V., Fischer, K.M., 2014. Contrasting lithospheric signatures across the western United States revealed by Sp receiver functions. Earth Planet. Sci. Lett. 402, 90–98.

Rychert, C.A., Shearer, P.M., 2009. A global view of the lithosphere-asthenosphere boundary. Science 324, 495–498.

Salmon, M., Kennett, B.L.N., Stern, T., Aitken, A.R.A., 2013. The Moho in Australia and New Zealand. Tectonophysics 609, 288–298.

Schaeffer, A.J., Lebedev, S., 2013. Global shear-speed structure of the upper mantle and transition zone. Geophys. J. Int. 194, 417-449.

Selway, K., Ford, H., Kelemen, P., 2015. The seismic mid-lithosphere discontinuity. Earth Planet. Sci. Lett. 414, 45–57.

Sippl, C., 2016. Moho geometry along a northsouth passive seismic transect through Central Australia. Tectonophysics 676, 56–69.

Sodoudi, F., Yuan, X., Kind, R., Lebedev, S., Adam, J.M., Kästle, E., Tilmann, F., 2013. Seismic evidence for stratification in composition and anisotropic fabric within the thick lithosphere of Kalahari Craton. Geochem., Geophys., Geosyst. 14, 5393–5412.

Sun, W., Kennett, B.L.N., 2016q. Uppermost mantle structure of the Australian continent from Pn traveltime tomography, J. Geophys. Res., Solid Earth 121, 2004–2019.

Sun, W., Kennett, B.L.N., 2016b. Receiver structure from teleseisms: auto- and cross-correlation, Geophys. Res. Lett. 43, 6234–6242.

Sun, W., Kennett, B.L.N., 2017. Mid-lithosphere discontinuities beneath the western and central North China craton, Geophys. Res. Lett., 44, 1302–1310.

Sun, W., Fu, L.-Y., Saygin, E., Zhao, L. (2018). Insights into layering in the cratonic lithosphere beneath Western Australia. J. Geophys. Res. Solid Earth, 123, doi: 10.1002/2017JB014904.

Tauzin B., Bodin T., Debayle E., Perrillat J.P., Reynard B., 2016. Multi-mode conversion imaging of the subducted Gorda and Juan de Fuca plates below the North American continent, Earth. Planet. Sc. Lett., 440, 135-146.

Tharimena, S., Rychert, C.A., Harmon, N., 2016. Seismic imaging of a mid-lithospheric discontinuity beneath Ontong Java Plateau, Earth Planet. Sci. Lett. 450, 62–70.

Thybo, H., 2006. The heterogeneous upper mantle low velocity zone. Tectonophysics 416, 53–79.

Thybo, H., Perchuc, E., 1997. The seismic 8° discontinuity and partial melting in continental mantle. Science 275, 1626–1629.

Warner, M., Morgan, J., Barton, P., Morgan, P., Price, C., Jones, K., 1996. Seismic reflections from the mantle represent relict subduction zones within the continental lithosphere. Geology 24, 39–42.

Wirth, E.A., Long, M.D., 2014. A contrast in anisotropy across mid-lithospheric discontinuities beneath the central United States - A relic of craton formation. Geology 42, 851–854.

Wittlinger, G., Vergne, J., Tapponnier, P., Farra, V., Poupinet, G., Jiang, M., Su, H., Herquel, G., Paul, A., 2004. Teleseismic imaging of subducting lithosphere and Moho offsets beneath western Tibet, Earth Planet. Sci. Lett. 221, 117–130.

Yoshizawa, K., 2014. Radially anisotropic 3-D shear wave structure of the Australian lithosphere and asthenosphere from multi-mode surface waves. Phys. Earth Planet. Inter. 235, 33–48.

Yoshizawa, K., Kennett, B.L.N., 2015. The lithosphere-asthenosphere transition and radial anisotropy beneath the Australian continent, Geophys. Res. Lett., 42, 3839-3846,

Yuan, H., and Levin V., 2014. Stratified seismic anisotropy and the lithosphere-asthenosphere boundary beneath eastern North America, J. Geophys. Res. Solid Earth 119, 3096–3114.

Yuan, H., Romanowicz, B., 2010. Lithospheric layering in the North American Craton, Nature 466, 1063–1068.

Zhu, L., 2000. Crustal structure across the San Andreas fault, southern California, from teleseismic converted waves, Earth Planet. Sci. Lett. 179, 183–190.